Sea Surface Velocities from Visible and Infrared Multispectral Atmospheric Mapping Sensor Imagery

P. A. Pope[1], W. J. Emery, AND M. Radebaugh[2]

Colorado Center for Astrodynamics Research, University of Colorado, Boulder

[1]Now at the Los Alamos National Laboratory, Los Alamos, New Mexico
[2]Now at TRW, California

Sea Surface Velocities from Visible and Infrared Multispectral Atmospheric Mapping Sensor Imagery

P. A. Pope, W. J. Emery, AND M. Radebaugh

Absract

High resolution (100m), sequential Multispectral Atmospheric Mapping Sensor (MAMS) images have been used in a study to calculate advective surface velocities using the Maximum Cross Correlation (MCC) technique. Radiance and brightness temperature gradient magnitude images were formed from visible (0.48 microns) and infrared (11.12 microns) image pairs, respectively, of Chandeleur Sound, which is a shallow body of water northeast of the Mississippi delta, at 145546 GMT and 170701 GMT on March 30, 1989. The gradient magnitude images enhanced the surface water feature boundaries, and a lower cutoff on the gradient magnitudes calculated allowed the undesirable sunglare and backscatter gradients in the visible images, and the water vapor absorption gradients in the infrared images, to be reduced in strength. Requiring high (>0.4) maximum cross correlation coefficients and spatial coherence of the vector field aided in the selection of an optimal template size of 10 x 10 pixels (first image) and search limit of 20 pixels (second image) to use in the MCC technique. Use of these optimum input parameters to the MCC algorithm, and high correlation and spatial coherence filtering of the resulting velocity field from the MCC calculation yielded a clustered velocity distribution over the visible

and infrared gradient images. The velocity field calculated from the visible gradient image pair agreed well with a subjective analysis of the motion, but the velocity field from the infrared gradient image pair did not. This was attributed to the changing shapes of the gradient features, their nonuniqueness, and large displacements relative to the mean distance between them. These problems implied a lower repeat time for the imagery was needed in order to improve the velocity field derived from gradient imagery. Suggestions are given for optimizing the repeat time of sequential imagery when using the MCC method for motion studies. Applying the MCC method to the infrared brightness temperature imagery yielded a velocity field which did agree with the subjective analysis of the motion and that derived from the visible gradient imagery. Differences between the visible and infrared derived velocities were 14.9 cm/s in speed and 56.7 degrees in direction. Both of these velocity fields also agreed well with the motion expected from considerations of the ocean bottom topography and wind and tidal forcing in the study area during the 2.175 hour time interval.

Introduction

The Maximum Cross Correlation (MCC) technique has been used for studies of cloud motion (Leese et al., 1971), pack ice motion (Ninnis et al., 1986 and Emery et al., 1991), and advective ocean surface motion (Emery et al., 1986; Vastano and Reid, 1985). The study by Emery et al. (1986) applied the MCC technique to gradients of infrared images from the Advanced Very High Resolution Radiometer

(AVHRR) instrument onboard the NoAA polar orbiter satellites, and the resulting advective velocities agreed well with the geostrophic mean and short-term wind-driven currents in the study area. Infrared and visible CZCS satellite sequential imagery has been used to subjectively compute advective surface currents from the displacement of sea surface patterns contained in the imagery (Vastano et al., 1985). Garcia et al. (1989) applied the MCC technique to CZCS visible imagery of the relatively shallow English Channel, and Svejkovsky (1988) applied the MCC technique to CZCS visible imagery and AVHRR infrared imagery. Both studies had good success. Svejkovsky's study showed that both the visible and infrared imagery yielded similar flows even though the upwelling radiance originated from differing depths.

The MCC method offers an objective means of calculating velocities from the displacement of surface features in sequential imagery. In the MCC method, cross-correlations between sequential images of sea surface features are computed in windowed portions of each image. A smaller template window in the first image is moved around within a larger search window in the second image. The search window's size is governed by the search limit, which is the maximum spatial lag used in calculating the cross correlation coefficients. The calculation of the cross correlation at all positions of the template within the search window defines a function whose maximum is deemed the position to which the template feature has moved during the time interval (Emery et al., 1986; Ninnis et al., 1986). This location is taken as the end of the vector of the surface current which had its origin at the center of

the search window. The calculation of velocities for template positions over the entire image array yields an advective velocity field. The size of the template and search windows may be optimized by requiring high values for the maximum cross correlation coefficients of the velocity vectors. Overlap between template windows provides sufficient coverage over the study area, and the resulting advective velocities can be compared with the motion calculated from a subjective analysis to judge the overall flow obtained by the MCC method.

Errors in the feature tracking and MCC methods may be due to the basic assumption that all of the changes between the images were due to horizontal advection. While this may be a limiting assumption over very long time periods it is not a bad assumption for the shorter time interval we have used in this study. It should be remembered, however, that there are competing mechanisms that can change the surface parameter fields being measured with the MAMS spectral channels. The surface feature motion of the thermal infrared channels can be influenced by heating/cooling and upwelling/downwelling (Wahl et al., 1990), while the visible images can be altered by in situ plankton blooms, biological consumption, sediment infusion, chemical changes at the ocean surface, as well as changes in wind speed, which affect sunglitter (Viollier et al., 1970). Finally, both visible and infrared images can be affected by diffusive changes which generally take longer than the short time intervals between successive images. All of these effects will introduce errors into the vector motion calculated from the sequential imagery.

One of the primary problems in computing motion from sequential satellite images is the limit of the polar orbiting satellites in terms of image repeat time. The shortest possible interval between AVHRR images is nominally 6 hours which in some cases may be much too long to resolve the motion experienced in the advection of the field sensed by the satellite system. The CZCS sampling only repeated every 24 hours, which severely restricted the viewing of changes between color images of ocean features. Cloud cover may impede the viewing of an area of interest by either of these systems on any pass. It would be attractive to have both infrared and visible images which were cloud free and more closely spaced in time to explore the limits of the MCC method. Also, more study is needed to understand the similarities and differences between the motions calculated from visible and infrared sequential imagery. Finally, the AVHRR and CZCS instruments have a minimal spread over the electromagnetic spectrum, and it has not been shown that these spectral ranges are the best ones for advective motion studies.

The airborne Multispectral Atmospheric Mapping Sounder (MAMS) instrument provides high resolution imagery in 12 channels, spanning the visible, near infrared, and thermal infrared regions of the electromagnetic spectrum (Jedlovec et al., 1989). The imagery in this work are cloud free, and MAMS imagery can have a predetermined repeat time, with a minimum repeat time of about 1 hour. The spectral range of the channels, the coverage, resolution, and the availability of a variable repeat time make the data useful for exploring the possibilities of tracking ocean motion.

In this report, the high spatial resolution, multispectral images from the MAMS instrument were used to explore the selection of spectral range, preprocessing of the sequential imagery, and choice of input parameters (template size and search limit) for computing the advective velocities of the sea surface features by the MCC method. The March 30 1989 passes over Chandeleur Sound offered sequential, cloud free imagery of a very dynamic coastal region. The flows obtained from the imagery can be useful for coastal ecology and sediment transport studies (Moeller et al., 1989) The spectral range covered by the the MAMS instrument made it possible to choose channels with strong surface feature signals and low image noise. Requiring high maximum correlation coefficients of the velocity vectors facilitated choosing an optimum template size and search limit. Spatial coherence filtering of the velocity field enhances the flow associated with translational displacements. Finally, a comparison of the advective velocity vectors obtained from the visible and infrared image pairs is presented.

Image Data Set

A. MAMS images

The MAMS instrument is an airborne Dadaleus scanning radiometer which is typically flown at an altitude of 20 kilometers, has a swath width of approximately 36 kilometers, and a spatial resolution of 100 meters. The MAMS instrument has twelve channels (two are spectrally redundant) spanning an electromagnetic range from the visible to the far infrared. Table 1 shows the bandwidths of the eight visible/near infrared channels and the four far infrared

channels. The MAMS data were collected, navigated, and remapped into a recti-linear projection such that the spacing between data elements is 100 meters. The navigation of the images offers a maximum registration accuracy of 200 meters. Detailed information on the MAMS instrument is contained in Jedlovec et al. (1989).

The images used in this study were from a March 30, 1989 flight over Chandeleur Sound and the Mississippi delta (Fig. 1). Chandeleur Sound is a shallow body of water northeast of the Mississippi delta and is bounded by a string of barrier islands and the Louisiana mainland. It is a highly dynamic region due to its proximity to the Mississippi delta which introduces cool, sediment rich water into the warmer, clearer waters of the sound. Also, the bottom topography of the area and the Chandeleur barrier islands make for interesting flow due to tidal forcing. Radiance data were available for channels 2 - 8, and brightness temperature data were available for channels 9 - 12. Grayscale images were formed from these data and limits on the data represented for each channel were set to optimize the useful signal. All of the visible imagery suffered from sunglare. This effect manifests itself as a smoothly varying increase/decrease in radiance values in a horizontal direction across the images. Deviations from this trend are caused by sunglint off surface waves. The visible blue light image of Fig. 2(a) has a large sunglare gradient on the eastern side of the image and a shallower gradient due mainly to Rayleigh backscattering on the western side. The infrared image of Fig. 2(b) has a very shallow gradient on both sides of the image due to water vapor absorption (C. Moeller, personal communication, 1991).

The resolution and time differences of these images allows a simple and convenient parameter to be defined. The speed of water features in the sequential images can be found by multiplying the spatial displacement in pixels by a characteristic speed, defined as,

$$C = r/\Delta t/ \text{ pixel} \qquad (1)$$

where r is the spatial resolution and Δt is the difference in time between the images. Since it is the speed associated with a single pixel displacement, it represents the lower limit on the range of speeds which can be calculated from perfectly coregistered imagery. The spatial resolution of the MAMS data is a constant 100 meters, so the time difference drives the characteristic speed for the MAMS imagery. The use of the characteristic speed in choosing temporal limits is discussed later. The time difference between the images of this study is 2.175 hours, yielding a characteristic speed of 1.28 cm/s/pixel.

B. Channel selection and gradient image formation

The channels to use in this motion study were subjectively selected by examining all the available images. Strong water feature signal and low noise were the criterion used. The visible/near infrared channels, 2 - 8, all showed the same basic water features; however, channel 2 had the strongest and finest water feature signal of all the visible channels. Unfortunately, this imagery also contained the most contamination due to atmospheric effects and sunglare. Channels 9 and 10, which are spectrally redundant, had too much striping and random noise to be useful. Channels 11 and 12 showed the same thermal water features, but channel 12 suffered more from random noise and striping than did

the channel 11 images (see Jedlovec et al., 1989). Thus, the channel 2 and channel 11 image pairs were selected as the visible and infrared images, respectively, to use in this study.

Similarity calculations such as the MCC method have been shown to work well when the edges of the features to be tracked are enhanced (Emery et al., 1986; and GE et al., 1987). As suggested by Emery et al. (1986), it is only the patterns in the sequential imagery which are to be tracked, and the infrared gradient magnitude images used in that study provided water feature boundaries from which the MCC method could yield a coherent vector field with high correlation values. This philosophy of attempting to track only sea surface patterns was adopted for the preprocessing of all the imagery in this study. Corrections for Rayliegh scattering and sunglint (visible channels) and water vapor absorption (infrared channels) was not done. Only a simple technique for handling these contaminations was attempted in an effort to show that the water surface features only need to be marked in some manner for tracking by the MCC technique. For motion studies, the more tedious calculations of reflectance and SST imagery also serves to provide a similar signal for any advecting sea surface feature in both pairs of imagery, as well as remove contamination. The land was masked from the images and they were smoothed using a 3 x 3 running median filter to remove small scale noise. The channel 11 images suffered from some striping noise which was reduced by passing a 5 x 5 running median filter over this image pair. Two passes of this filter eliminated the striping noise while still preserving the large scale thermal features of interest. The strong sunglare signal present in

the eastern part of the visible image pair prompted exclusion of this area from analysis. Since the visible and infrared motions are to be compared, this same area was also excluded from the motion analysis with the infrared image pair. Gradient images were formed by applying a weighted central difference calculation to the smoothed channel 2 and channel 11 images. The magnitude of the gradient is given by,

$$|G(i,j)| = (1/2d)[(P(i-1,j) - P(i+1,j))^2 + (P(i,j-1) - P(i,j+1))^2]^{1/2} \quad (2)$$

where P(i,j) is the gray scale value at position i,j in the image array and d was chosen as 1 pixel (100 m). The maximum and minimum values of | G(i,j) | were found for each image and used to scale the gradient magnitude values to grayscale values. The results for a channel 2 image and a channel 11 image are given in Fig. 3(a) and (c) respectively. The full range of gradient magnitudes is represented in these "total" gradient images. The visible and infrared gradient image pairs contain gradients due to the surface water features to be tracked ("primary" gradients), as well as those due to various contaminations ("secondary" gradients). The primary gradients of the visible imagery are mainly due to boundaries between various direct and resuspended sediment loadings and those of the infrared imagery are due to thermal gradients. The secondary gradients in the visible image pair are due to sunglare/sunglint and Rayleigh scattering effects (backscatter), while those of the infrared image pair are due to atmospheric absorption. These secondary gradients appear as wavy vertical lines in Fig. 3(a) and (c). Note that the

secondary gradients due to sunglare on the eastern side in Fig. 3(a) are closely spaced while those due to backscatter on the western side are spaced farther apart. The secondary gradients due to atmospheric absorption in Fig. 3(c) are widely spaced and apparent only in certain regions of the image. The spacing of all the secondary gradients is an indication of the relative strength and spatial extent of their associated contaminations. The gradient magnitudes of the backscatter contamination in the visible gradient imagery were found to be lower than those of the primary gradients which were to be tracked. The secondary gradients due to this atmospheric contamination were eliminated by setting a subjective lower limit on the gradient magnitudes represented (Fig. 3(b)). The cutoffs for each of the visible full gradient images were chosen to be the point at which most of the secondary gradients were eliminated from the images with minimal effect on the primary gradients. This lower cutoff was an average of 0.28 $mW/cm^2/st/\mu m/pixel$ for both images. The secondary gradients due to sunglare were of approximately the same value as some of the stronger primary gradients, and so, could not be totally eliminated with this simple technique. As previously mentioned, this part of the imagery is excluded from analysis. Lower cutoffs were also used on the infrared gradient imagery to eliminate the secondary gradients due to atmospheric absorption (Fig. 3(d)). The magnitudes of the secondary gradients were close in value to the primary gradient magnitudes, and so, it was more difficult to choose a lower gradient magnitude cutoff without eliminating the primary gradients. The lower cutoff was an average of 0.32 Kelvin/pixel for

both infrared full gradient images. A higher cutoff on the gradients was used to eliminate the extremely high gradient magnitudes which occurred very close to the shore, since they biased the scaling of the real valued gradient magnitudes to integer values. The gradient magnitude calculation with appropriate high and low cutoffs was applied to the channel 2 and 11 MAMS images and these two pairs of images served as the input arrays for the MCC calculation.

The gradient images for the channel 2 and 11 MAMS data, Fig. 3(b) and (c), are different in several ways, and a comparison of them is appropriate here. The gradient image pair for the visible data shows a relatively sparse field of gradient features, which are very linear, and well defined. They were found to be approximately 1 to 2 kilometers in length (10 to 20 pixels). Also, residual solar glare noise still exists on the right side of the image for the second time image. In contrast, the gradients of the infrared images are longer in extent and many of them changed shape, or "warped", between the two times. Several positions for gradient features were present in both the visible and infrared gradient image pairs. These gradient features will provide vectors from which an objective comparison of the two flows can be calculated. The gradient features in the Chandeleur Sound region were different for the visible and infrared gradient images. The gradient magnitudes calculated for the infrared image pair were similar in value for this region, as evidenced by the small range in grayscale values of the gradient features. This was not as true for the visible image pairs which showed a wide range of grayscale values for the gradient features. This difference is mostly due to the smaller spatial variability of

thermal features in this region. The infrared imagery has its greatest thermal feature variability where the cool Mississippi river waters are mixing with the warmer waters of Chandeleur Sound. This boundary is denoted by a very strong, chevron shaped gradient feature in both types of gradient imagery (see Fig. 3(b) and (d)). Note also that the gradients on either side of this boundary are very different for the visible and infrared gradient images. The visible gradient imagery is relatively devoid of gradients on either side of the boundary, while the infrared gradient imagery has a great deal of structure on the southern side. Both the visible and infrared gradient imagery have very incoherent gradient feature displacements on the southern side of this boundary. The width of gradient features in the visible imagery was greater than that of the infrared imagery. This effect is probably due to diffusion of the sediment laden water into relatively clearer water. Both infrared gradient image pairs contained small gradients which were present at one time and not the other. These were mainly residual artifacts from the simple contamination removal technique previously discussed. Animation of the gradient imagery allowed investigation into the displacement characteristics of these flow tracers. Most of the gradient features in the visible gradient image pair simply translated and did not warp. The MCC algorithm works well when the features tracked are distinct, invariant, and translate (Ninnis, et al., 1986; Emery, et al., 1986). The warping, fading, and disappearing/reappearing aspects of the gradient images cannot be tracked by the MCC method, and will introduce errors in the velocity field calculated.

Due to the displacement problems mentioned above, feature tracking has an advantage over the MCC calculation because the human eye is able to discern patterns and rotational motion more accurately. This subjective method of obtaining advective velocities is obviously dependent on the individual performing the calculation, but it can offer a check on the general motion calculated by the objective MCC technique (see Emery et al., 1991). The gradient image pairs for channel 2 and 11 were used to calculate subjective velocity fields. Fig. 4(a) and (b) show the eighty vectors calculated for each channel. The mean speeds calculated were 18.6 and 23.0 cm/s for the visible and infrared gradient image pairs, respectively. Note that these speeds imply a mean displacement of 14 and 18 pixels for the visible and infrared gradient image pairs. This analysis served as a check on the general flow field calculated using the MCC technique and the requirements of high maximum cross correlations and spatial coherence.

The Maximum Cross correlation method

A. Definitions

In depth explanations of the Maximum Cross Correlation technique (matched filtering) can be found in the studies done by Emery et al. (1986), Ninnis et al. (1986), and Wahl et al. (1990). The discussion below concentrates on the effects of varying the template and search limit size inputs to the MCC algorithm. These inputs are the most important ones because they govern the size of the template window (first image) and the search window (second

image), and so, they influence the size of the pattern tracked and the maximum extent to which the pattern is expected to move.

A square array of pixel values in the first image array, A_1, at position i,j defines a template, (Fig. 5(a)). The template window, n x n, generally contains some feature whose velocity is desired. The cross correlation value is calculated for every position, or spatial lag value, of the template within the search window, m x m, of the second image array, A_2. This process yields a three dimensional cross correlation function whose maximum occurs at a relative position I',J'. Multiplying the relative displacement vector by the characteristic speed gives the velocity vector of the feature contained within the template. The direct cross correlation algorithm takes more computer time to calculate as compared to the fast Fourier transform of this method (Leese et al., 1971), but it allows for greater variations in the template size and search limit. Since one of the objects of this work was investigating the optimization of the input parameters, freedom to vary these was chosen over great computational speed.

The search window bounds the spatial extent of the cross correlation calculation within A_2. The size of the search window is governed by the search limit, L, imposed on the MCC calculation. The length of a side of the search window, m, is equal to twice the search limit plus the length of a side of the template. Since the template size governs the spatial extent of the patterns to be tracked, the resulting velocity field will be indicative of the advection of this size of feature in the imagery. If a characteristic size is intrinsic to the imagery, or if a particular size of pattern is

to be tracked, the size of the template should be chosen as this length. The size of the search limit will govern how far the template pattern is moved in calculating cross correlations. Thus the search limit size should be chosen as the greatest distance to be tracked in the imagery. In this way, the fastest moving features can be tracked by the MCC method, as well as smaller displacements. This argument for the determination of the search limit size is dependent on the uniqueness of the template pattern as compared to surrounding templates within the search limit size. If similar template patterns in the second image are within a search limit distance of the template pattern to be tracked from a given position, a false high cross correlation may be calculated, and, depending on the degradation of the original pattern, may result in an incorrect calculated displacement for the pattern being tracked. Overlaping templates provides adequate spatial coverage over the image (Fig. 5(b)). A velocity vector is calculated by the MCC method for each of the template positions and constitutes the velocity field output from the algorithm.

B. Optimization of MCC input parameters

Inputs to the MCC calculation include the spatial resolution of the image arrays and the time difference. These are governed by the data set available; however, the template size and the search limit are parameters which must be adjusted with the goal of obtaining a velocity field which is coherent, has high, maximum cross correlation coefficients, and motion which is consistent with the subjective analysis. As pointed out by Ninnis et al. (1986) , the use of the MCC method yields maximum cross correlation coefficients

which in general are less than one; i.e. the two images are not perfectly correlated. The MCC method was applied to the channel 11 gradient image pair to optimize the input parameters because it offered more gradient features to track than the channel 2 images, and as previously mentioned, the channel 11 gradient magnitude images showed more warping of the gradient patterns, which the MCC method cannot track well. It was anticipated that these images would require the most work in optimizing the input parameters. The channel 2 gradient magnitude images had gradient patterns which were very linear, and appeared to simply translate; features and motion the MCC method handles well. The optimization of the input parameters for the MCC calculation was performed for the infrared gradient magnitude images with the assumption that the optimal values obtained would work well with the visible gradient image pair also.

Variations in template size and search limit formed a matrix of runs from which the most optimal values could be found. Overlap values were varied to keep the number of vectors calculated near a common value for the following histogram analyses. The template sizes tried were 5, 10, 20, 30, and 40 pixels, and the search limits tried were 5, 10, 15, 20, and 30 pixels, forming a matrix of 25 runs. Since high maximum cross correlation coefficients are a requirement, histograms of the maximum cross correlation coefficients, and speeds were created from the runs to aid in choosing the optimal input parameters.

The variation in template size caused the peak of the correlation value histograms to shift toward lower values, regardless of the

search limit size used (Fig. 6). Also, the vector fields produced became less spatially coherent, and the vectors calculated were inconsistent with the subjective analysis. The highest correlations came from 5 x 5 and 10 x 10 template sizes. The most coherent vector field came from a template size of 10 x 10 pixels, which is close to the size of the gradient features seen in the image pairs. This template size contains 100 values for the cross correlation calculation, and so, is statistically more significant than the 25 values contained in the 5 x 5 template. The larger template sizes, while offering more points for the cross correlation calculation, also allow the inclusion of neighboring gradient features which have differing motions, and leads to an inaccurate velocity vector being produced (Ninnis et al., 1986). This suggests that the template size should be kept close to the size of the features to be tracked.

With the template size fixed at 10 x 10 pixels, the variation of the maximum cross correlation coefficients with variation in search limits could be examined. The maximum motion was varied from 5 to 40 pixels, corresponding to a range in speeds of 6.4 to 51.2 cm/s. The peaks in the maximum cross correlation histograms shifted toward higher values with an increase in search limit size. The shift was most pronounced between search limit sizes of 5 and 15 pixels, and did not shift significantly for the higher values (Fig. 7). The shift can be explained by considering the fact that, as the template is given more room to search for a maximum cross correlation value, the chance of finding a high correlation is increased as the search limit approaches the mean displacement distance of the features being tracked. Increasing the search limit

past the distance translated by most of the features in the images resulted in no significant improvement of the maximum cross correlation coefficients because the maximum cross correlation had been found at a smaller length scale. Thus, it is suggested that the search limit be chosen as the mean displacement expected or occurring in the sequential imagery. The optimum template size was chosen to be 20 pixels. This choice is consistent with the earlier result from the subjective motion analysis, where mean displacements of 14 and 18 pixels were found for the visible and infrared gradient imagery.

C. Velocity field results

A note on the effects of the navigation accuracy of the imagery is needed before quantitative velocity results are presented. As previously mentioned, any motion study is critically dependent on the extent to which the sequential imagery is coregistered (see for example Garcia et al., 1989). Registration inaccuracies introduce errors into the velocities calculated. The MAMS imagery has a misregistration error of 2 pixels (200 m). The product of the characteristic velocity and this misregistration yields an error of 2.56 cm/s for the speeds calculated in this study. The minimum error in direction for this study may be estimated by considering a feature which is displaced by a distance equal to the optimum search limit. This gives an error of 5.7 degrees. The maximum error would occur for a displacement of one pixel, in which the error in direction is 63 degrees.

The MCC algorithm was applied to the channel 2 and channel 11 gradient image pairs with the optimal template size and search

limits discussed. The vector fields were filtered such that only vectors with a correlation higher than 0.4 were plotted (Ninnis et al., 1986; Emery et al., 1986). This was chosen by inspection of the maximum cross correlation histogram associated with the optimal template size and search limit sizes previously discussed (Fig. 6). A more objective significance test has been used by others (see for example Garcia et al., 1989). Finally, these vector fields were filtered for spatial coherence. The spatial coherence filter compares a vector's length and direction against its nearest neighbors. If the vector's length and direction are within predefined limits for a certain number of neighboring vectors, the vector is kept; otherwise, it is discarded (Emery et al., 1991). Three nearest neighbors were used for the spatial coherence filtering, and the limits on length and direction were 4 pixels, or 1.28 x 4 = 5.12 cm/s, and 45 degrees, respectively. These limits are somewhat restrictive, and were chosen to enhance the translational displacements of the sea surface features. The results for the visible and infrared gradient image pairs are in Fig. 8(a) and (b) respectively. The clustering of vectors is an indication of localized flows for particular gradient features.

Overlaying the resulting vector fields with the gradient images and animation of the images with a computer graphics display system allowed an inspection of the velocities calculated by the MCC method. Inspection of the visible gradient derived flow showed that the majority of the vectors calculated faithfully represented the motions seen. Few vectors strayed from the gradients they were supposed to be tracking. A comparison of Fig. 4(a) and Fig. 8(a)

shows that the flows are similar. This was not true of the infrared gradient derived flow, as evidenced by Fig. 4(b) and Fig. 8(b). Close inspection of the images showed that stray vectors occurred when gradients were close with respect to the search limit of 20 pixels. The denser gradient features of the infrared image pair caused more inconsistencies in the velocity field calculated from this imagery than from the visible imagery. This suggests that the MCC technique is most useful for tracking features whose motion is small when compared to the spatial density of the sea surface features. The inconsistancies in both vector fields were greatest for the dense gradient region near the Mississippi delta. The maximum cross correlation coefficients of vectors in this region were found to be lower than those calculated for Chandeleur Sound. As previously mentioned, the gradient magnitudes in the infrared gradient imagery were similar in value, which robs the MCC technique of information in calculating the cross correlation between signals. It effectively reduces the cross correlation to one of shape instead of shape and value. The 5 x 5 median filter used on the infrared imagery to reduce striping aggravated this problem. One feature in the northwest corner of both the visible and infrared imagery was moving very fast, and inspection of it's motion revealed a speed of 38 cm/s, which could not be tracked with the 20 pixel search limit. A rerun of the MCC calculation with a search limit of 30 pixels produced vectors which tracked this feature, but the vector field did not faithfully reproduce the more abundant and smaller motions.

The displacement of features in sequential imagery is dependent on the repeat time, during which physical processes advect the sea

surface features. Smaller displacements would be expected from a shorter repeat time. This could result in a better velocity field for two reasons. As previously discussed, the MCC method works best for features which do not warp or rotate, and lowering the repeat time would naturally lower the occurrence and magnitude of these phenomena. Secondly, a smaller repeat time would require a lower search limit for the MCC analysis, and lessen the likelihood of calculating high maximum cross correlations due to an excessively large search window size, as shown in the optimization analysis of the MCC input parameters. This previous discussion would suggest that, for any given radiometer (fixed spatial resolution), a higher characteristic speed for the imagery gathered is more desirable than a lower one; however, lowering the repeat time must be tempered by the aforementioned fact that there is a limit to the coregistration of the sequential imagery, which introduces an uncertainty in the speeds calculated (Svejkovsky, 1988). A general formula for the optimal repeat time could be written as,

$$\Delta t = r\,R\,/\,V \qquad (3)$$

where r is the spatial resolution, V is the maximum speed to be resolved by the MCC method, and R is the mean distance between features in the imagery. This formulation suggests that the more dense the sea surface features are, the shorter the repeat time required to efficiently extract the motion from the imagery.

In an attempt to obtain a more coherent velocity field from the infrared imagery, the MCC method with the optimized input parameters previously discussed was applied to the infrared brightness temperature image pair. No correction was made for the

water vapor absorption because, as previously mentioned, it was a very small effect. Still, this will introduce some errors into the motion calculation. There was an overall brightening in the relative grayscale values of the second image as compared to the first. This brightening of the infrared imagery was due to air-sea heat exchange, and caused a shift in the mean of the grayscale values (brightness temperature values). This effect does not influence the MCC calculation to a great extent, because the template and associated search window patterns are "demeaned" during the calculation of the cross correlation coefficient, as explained by Wahl et al. (1990). Application of the high correlation and spatial coherence filters resulted in a much improved velocity field. Figures 9(a) and (b) show that the visible and infrared derived flows are very similar. A comparison of Fig. 4(b) and 9(b) shows that the objective and subjective motion analyses yielded similar flows, as expected. Histograms of the calculated speeds gave an average speed of 13.9 cm/s with an average deviation of 8.6 cm/s for the visible gradient velocity field, and an average speed of 16.8 cm/s with an average deviation of 7.5 cm/s for the infrared brightness temperature velocity field. Figure 10(a) and (b) shows the visible gradient and infrared brightness temperature derived flows overlayed on their respective imagery.

Since, these two flows were seen to be similar in a subjective manner, an objective comparison was performed. The velocity fields derived from the visible gradient and infrared brightness temperature imagery were differenced. Only template positions which had a vector from both flow fields were used in the

calculation. Histograms of the range of differences in the speeds and relative directions were formed to judge the similarity of the two flows. The average difference in speeds was -0.36 cm/s with an average deviation of 6.6 cm/s and a standard deviation of 9.3 cm/s. The average difference in relative direction was -18.4 degrees with an average deviation of 67.2 degrees and a standard deviation of 97.0 degrees.

The velocity fields calculated by both the feature tracking and the MCC methods show a general northwesterly flow in Chandeleur Sound, and a southerly flow of water around the northern tip of the main Chandeleur Island. The flow at the northern end of the islands seems to be competing with the more predominant northern flow in the Sound. The bathymetry information for the Chandeleur Island area shows a sharp southeasterly gradient at the southern end of the island chain, and a shallower easterly gradient at the northern end. The relative shallowness of Chandeleur Sound (typically 4 meters) suggests that wind and tidal forcing would have the greatest influence on this body of water. Sea level and wind speed/direction data collected in the study area on March 30, 1989 were used to investigate the relative strength of these two forces.

During the time the images were collected, the sea level was approaching high tide, with a height increase of approximately 10 cm during the time the images were taken, and a rate of change in sea level of 4.8 cm/hr. The wind direction was West Northwest and constant prior to, and during the time interval of the study; however, the winds were strong prior to the first scan. The wind speeds were 15 knots three hours before the first scan, and relatively calm at 6

to 8 knots during the two scans of the area. The step-like function of the wind speed prior to the scans suggests that inertial currents should exist. These currents should manifest themselves as anticyclonic eddies, but only one eddy was seen in the image, and its position at the tip of one of the Chandeleur Islands suggests this is due only to the island's interaction with the flow. The shallowness of Chandeleur Sound may have resulted in enough drag to dissipate any inertial currents due to wind forcing prior to the MAMS passes. In addition, the study area was under the influence of a cold front which had passed through the area the day before. This change in atmospheric conditions could be a source of error in the infrared imagery which is affected by water/air heat flux coupling. Thus, tidal forcing seems to be the main factor influencing the flow calculated from the sequential imagery of this study. The incoming tidally forced currents from the Gulf of Mexico would be turned from their northwesterly flow into Chandeleur Sound by the sharp topography gradient present at the southern end of the island chain. This topography gradient would also increase the speed of the flow into the Sound.

Conclusions

The MCC method has been successfully applied to gradient magnitude images of visible and infrared sequential MAMS imagery to detect the advective motion of sea surface features. The analysis suggests that the signals of channels 2 (0.48 micron) and 11 (11.12 micron) are sufficiently strong to provide tracers for advective sea

surface flow calculations by the MCC method. The calculation of gradient magnitude imagery offers a simple preprocessing technique for reducing atmospheric and sunglint contamination of visible imagery while preserving those gradients which may be used as tracers of advective flow. The visible image gradients were sparse, but distinct and very linear, and did not warp as much as the infrared image gradients. A template size of 10 x 10 pixels and a search limit of 20 pixels, which are close to the most common size and displacement of the gradient features, respectively, yielded velocity vectors with high maximum cross correlation coefficients. Spacial coherence filtering enhanced the translational motion of the gradient features. The velocity fields calculated from the visible and infrared imagery were in good agreement with each other and a subjective analysis of the motion. Errors in the velocity fields calculated by the MCC technique were incurred due to the dense gradient population of the infrared gradient image pair and the region near the Mississippi delta in both the visible and infrared gradient imagery. A lower repeat time for the sequential imagery is suggested to improve the velocity vectors calculated from application of the MCC method to gradient imagery.

Acknowledgements. Discussions with Gary Jedlovec of the Marshall Space Flight Center, and Chris Moller, of the Space Sciences Center, University of Wisconsin, were very helpful in interpreting the multitude of features in the MAMS images. The MCC code and some of the preprocessing codes were written by Chuck Fowler, to whom special thanks is given. MAMS data acquisition and image navigation

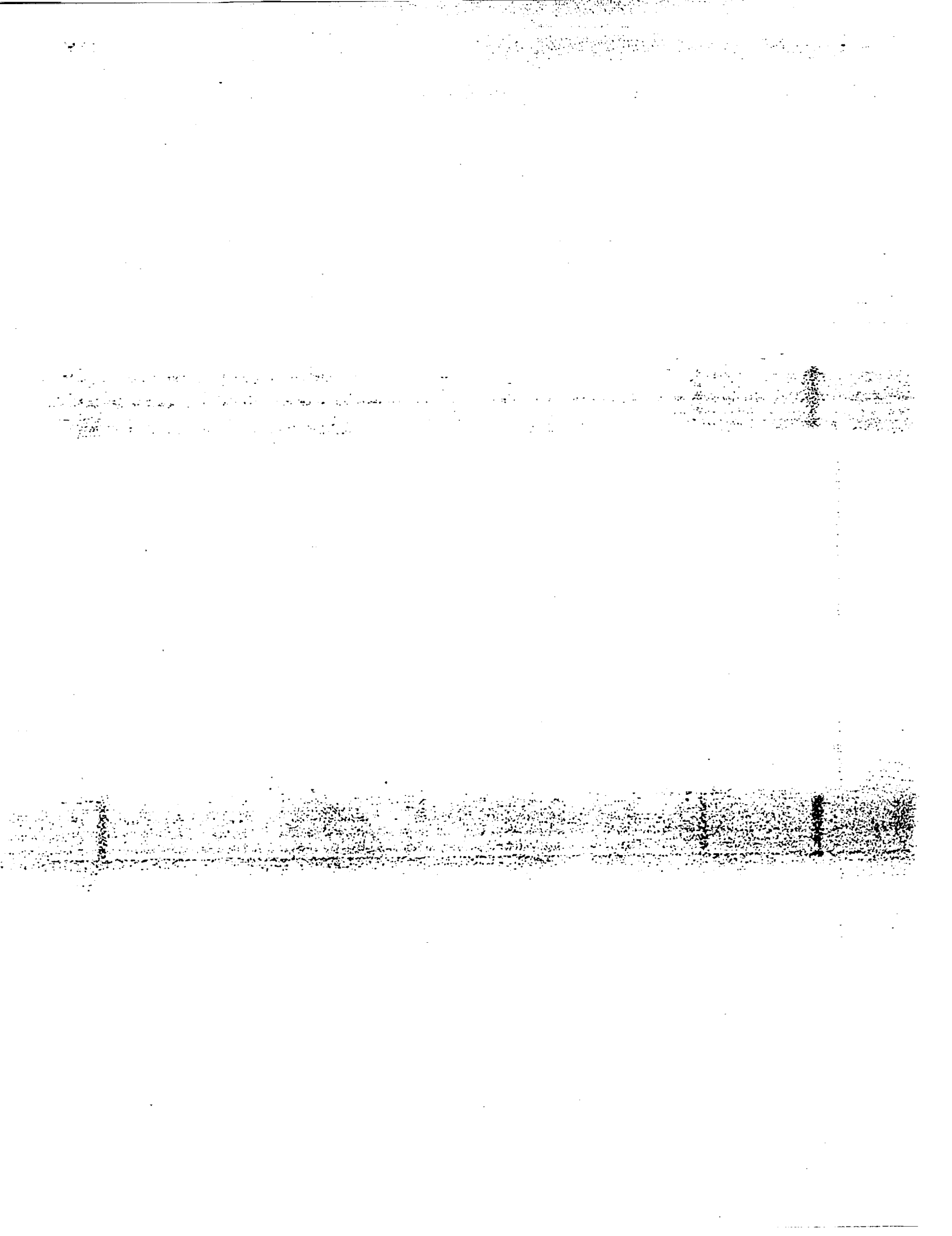

were performed by the Marshall Space Flight Center. This research was supported by NASA Grant NAG 8-806; this support and the interest of Jim Dodge at NASA headquarters is gratefully acknowledged by the authors.

REFERENCES

Emery, W. J., C. W. Fowler, J. Hawkins, and R. H. Preller, Fram Strait satellite image-derived ice motions, *J. Geophys. Res.*, 96, 4751-4768, 1991.

Emery, W. J., A. C. Thomas, M. J. Collins, W. R. Crawford, and D. L. Mackas, An objective method for computing advective surface velocities from sequential infrared satellite images, *J. Geophys. Res.*, 91, 12,865-878, 1986.

Garcia, C. A. E., and I. S. Robinson, Sea surface velocities in shallow seas extracted from sequential Coastal Zone Color Scanner satellite data, *J. Geophys. Res.*, 94, 12,681-12,691, 1989.

General Electric, Automated mesoscale winds determined from satellite imagery, GE Report 83HV002, General Electric Company, Automated Systems Department, Huntsville Center Operations, Hunstville, AL, 50pp., 1987.

Jedlovec, G. J., K. B. Baston, R. J. Atkinson, C. C. Moeller, W. P. Menzel, and M. W. James, Improved capabilities of the Multispectral Atmospheric Mapping Sensor (MAMS), NASA Technical Memorandum 100352, Marshall Space Flight Center, Huntsville, AL, 71pp., 1989.

Leese, J. A., C. S. Novak, and B. B. Clark, An automated technique for obtaining cloud motion from geosynchronous satellite data using cross correlation, *J. Appl. Meteorol.*, 10, 118-132, 1971.

Moeller, C. C., L. E. Gumley, K. I. Strabala, and W. P. Menzel, High resolution depiction of SST and SSC from MAMS data, Fourth Conference on Satellite Meteorology and Oceanography, AMS, Boston, 208-212, 1989.

Ninnis, R. M., W. J. Emery, and M. J. Collins, Automated extraction of pack ice motion from AVHRR imagery, *J. Geophys. Res.*, 91, 10,725-734, 1986.

Svejkovsky, J., Sea surface flow estimation from Advanced Very High Resolution Radiometer and Coastal Zone Color Scanner satellite imagery: a verification study, J. Geophys. Res., 93, 6735-6743, 1988.

Vastano, A. C., S. E. Borders, and R. E. Wittenberg, Sea surface flow estimation with infrared and visible imagery, *J. Atmos.Technol.*, 2, 401-403, 1985.

Vastano, A. C., and R. O. Reid, Sea surface topography estimation with infrared satellite imagery, *J. Atmos. Ocean. Technol.*, 2, 393-400, 1985.

Viollier, M., D. Tanre, and P. Y. Deschamps, An algorithm for remote sensing of water color from space, *Boundary Layer Meteorol.*, 18, 247-267, 1980.

Wahl, D. D., and J. J. Simpson, Physical processes affectng the objective determination of near-surface velocity from satellite data, *J. Geophys. Res.*, 95, 13511-13,619, 1990.

Figures

Fig. 1 Coastline map and selected bathymetry for Chandeleur Sound, Mississippi delta, and surrounding region.

Fig. 2 Visible radiance and infrared brightness temperature images for MAMS (a) channel 2, and (b) channel 11 at 170701 GMT on March 30, 1989. The land has been masked in black. Radiance values of 2.5 to 8.5 $mW/cm^2/st/\mu m$ and brightness temperature values of 289 to 305 Kelvin are represented in these visible and infrared grayscale images, respectively.

Fig. 3 Gradient magnitude images formed from MAMS visible and infrared imagery at 145546 GMT. (a) "Full" and (b) "primary" gradient image for channel 2, and (c) "full" and (d) primary gradient image for channel 11. The gradient magnitudes represented in the primary gradient imagery are 0.28 to 3.6 $mW/cm^2/st/\mu m$ per 100 meters for the visible, and 0.32 to 6.3 Kelvin per 100 meters for the infrared.

Fig. 4 Subjective velocity fields calculated from a feature tracking analysis of (a) the channel 2 and (b) the channel 11 "primary" gradient image pairs.

Fig. 5 (a) Graphical depiction of input arrays and parameters for the MCC method. (b) Template positions for the application of the

MCC method in the study area with the optimal inputs discussed in the text. A velocity vector will be calculated for each of the 7448 positions shown.

Fig. 6 Histograms of maximum cross correlation coefficients for a search limit size of 20 pixels and various values of template size.

Fig. 7 Histograms of maximum cross correlation coefficients for a template size of 10 x 10 pixels and various values of the search limit.

Fig. 8 Velocity field results from the MCC calculation using (a) visible gradient, and (b) infrared gradient image pairs. High correlation value and spatial coherence filtering have been applied.

Fig. 9 Velocity field results from the MCC calculation using (a) visible gradient, and (b) infrared brightness temperature image pairs. High correlation value and spatial coherence filtering have been applied.

Fig. 10 Velocity field results from Figure 9 overlayed on the associated visible gradient (a) and infrared brightness temperature imagery for 145546 GMT.

Table 1. MAMS channels and spectral bandwidths

MAMS channel	Bandwidth at 50 % response (microns)
1(a)	0.42 - 0.45
2	0.45 - 0.52
3	0.52 - 0.60
4	0.57 - 0.67
5	0.60 - 0.73
6	0.65 - 0.83
7	0.72 - 0.99
8	0.83 - 1.05
9(b)	3.47 - 3.86
10	3.47 - 3.86
11	10.55 - 12.24
12	12.32 - 12.71

(a) Channel 1 is not available when 10 bit infrared data is collected
(b) Channels 9 and 10 are redundant

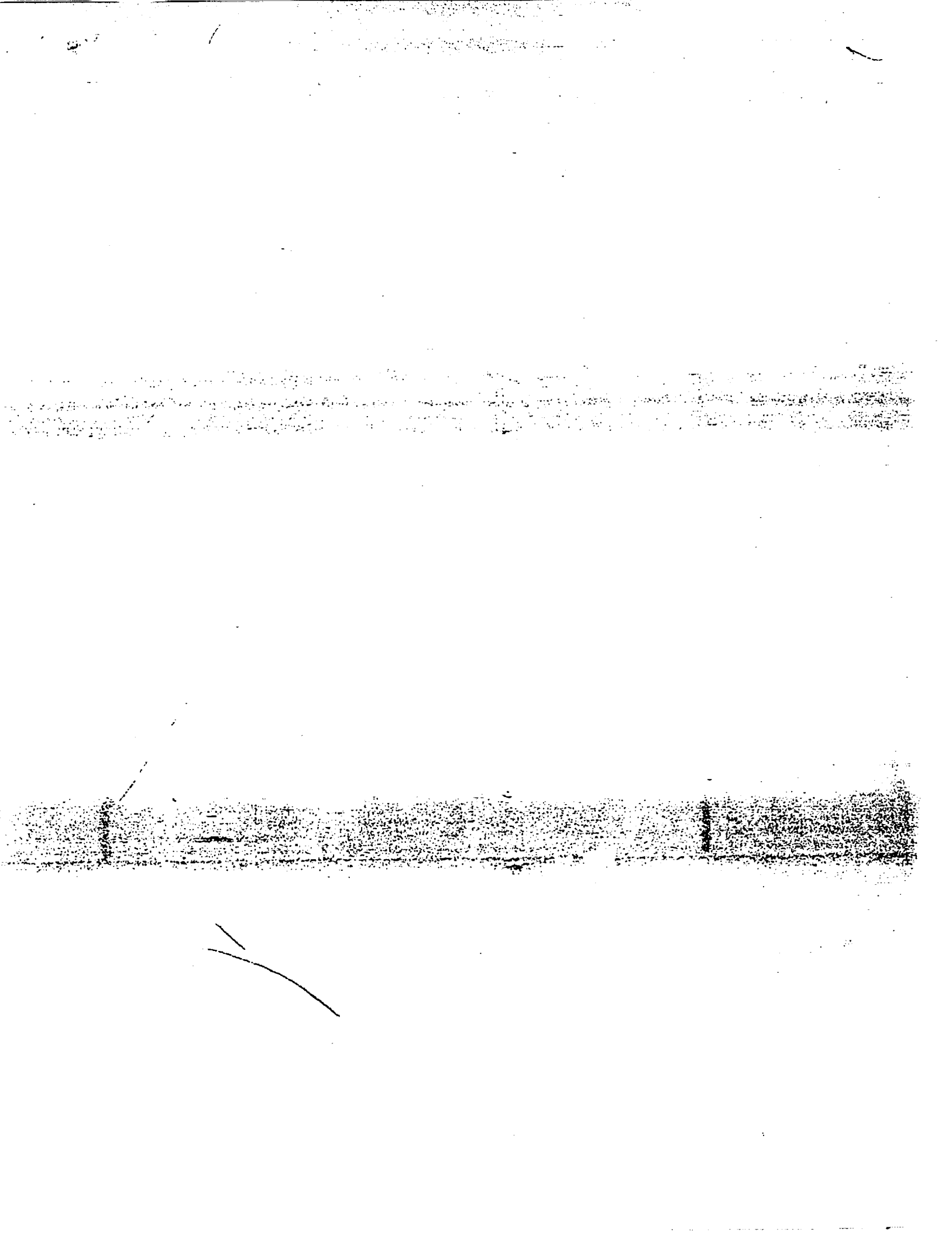

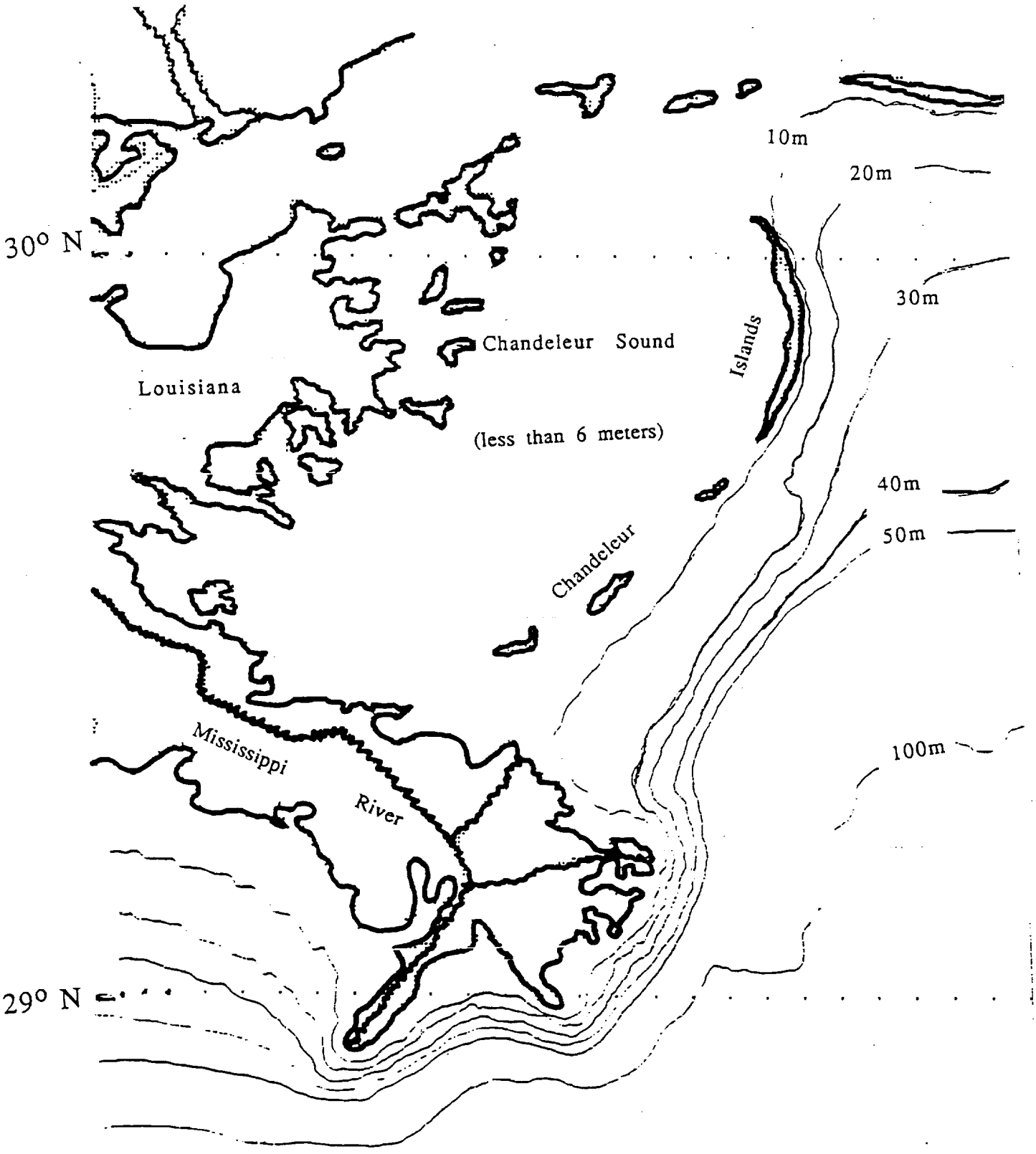
10m
20m
30m
40m
50m
100m
30° N
29° N
Chandeleur Sound
Islands
Louisiana
(less than 6 meters)
Chandeleur
Mississippi
River

Figure 1

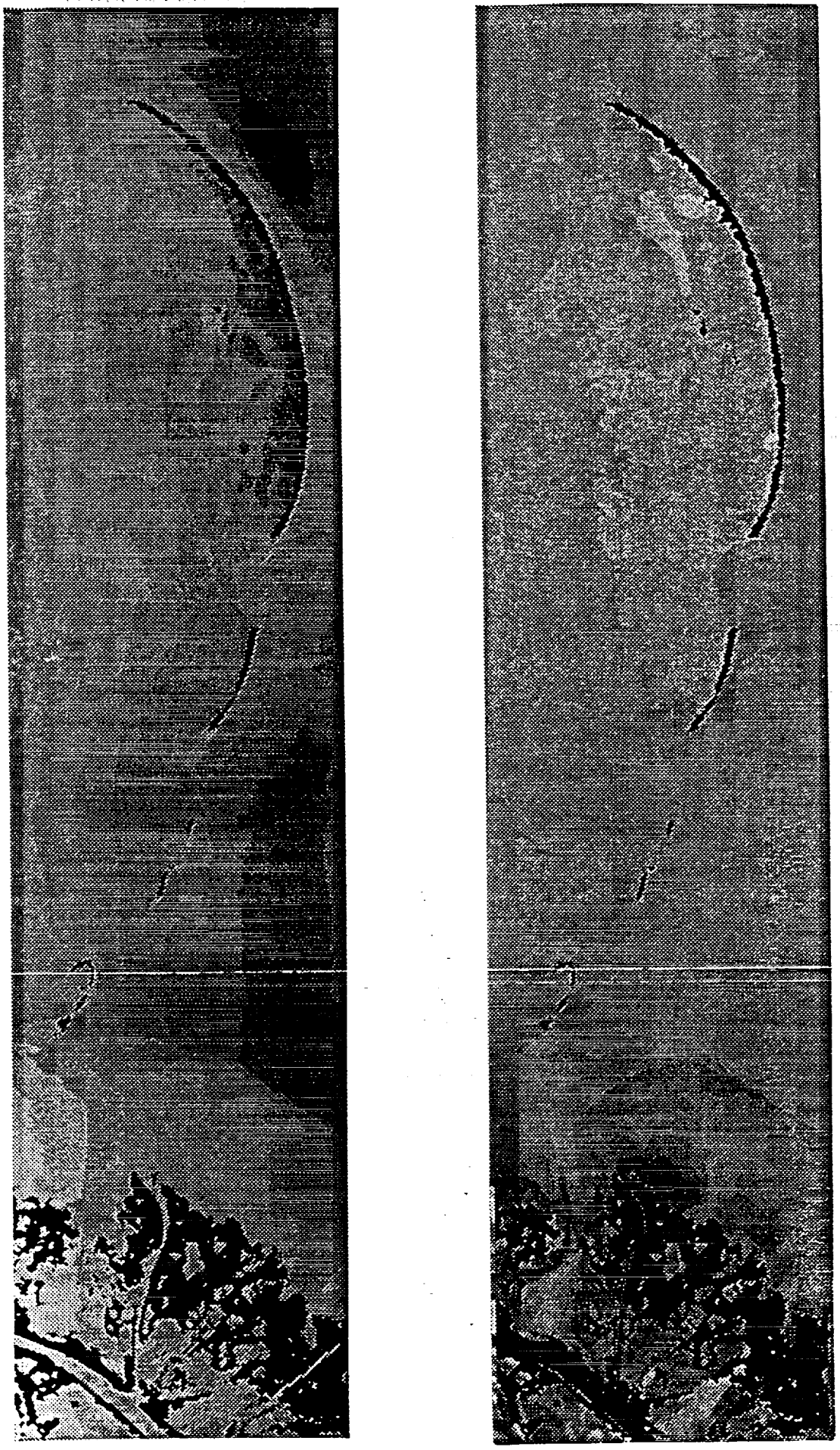

(a) (b)

Figure 2

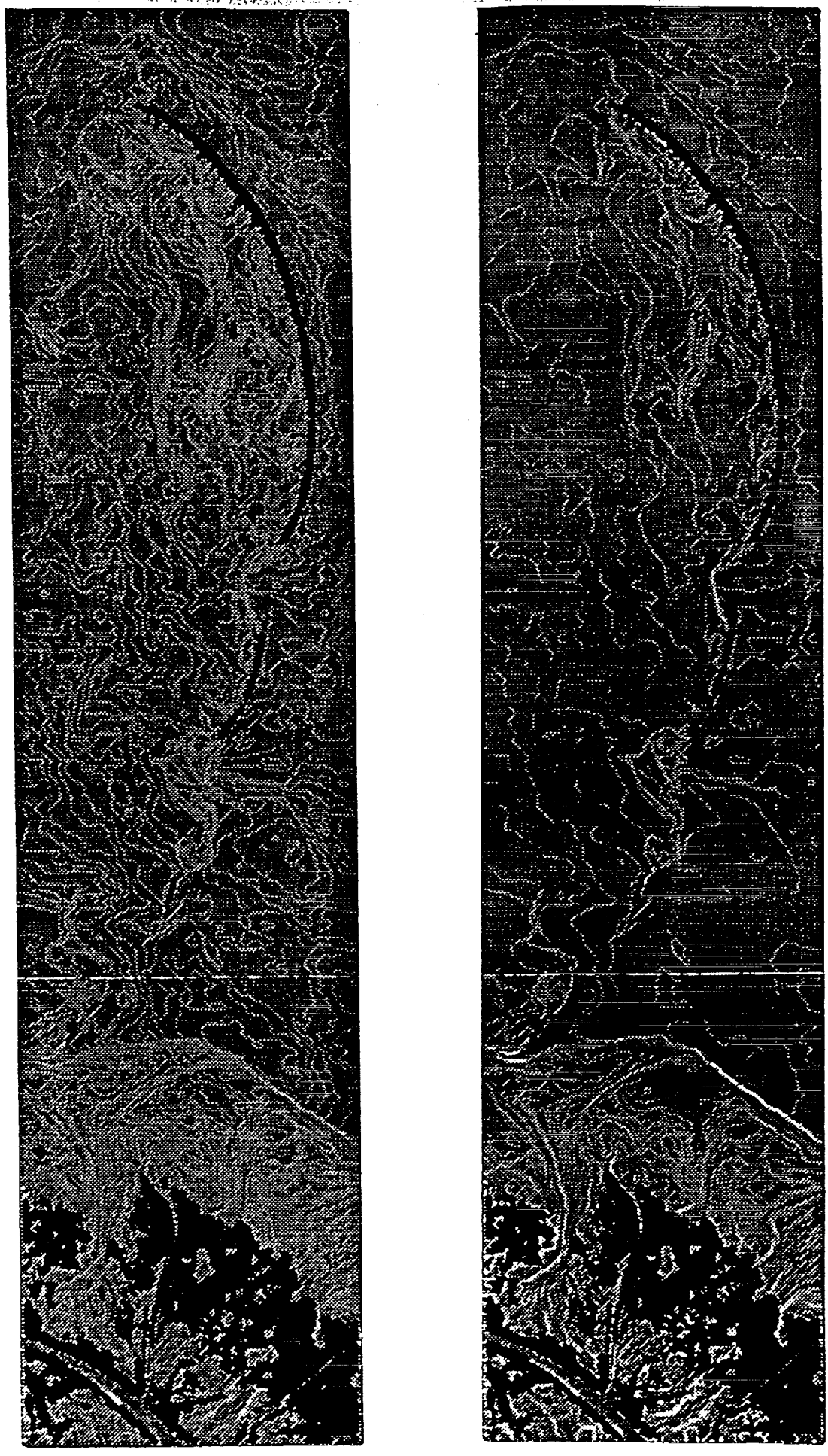

(c) (d)

Figure 3

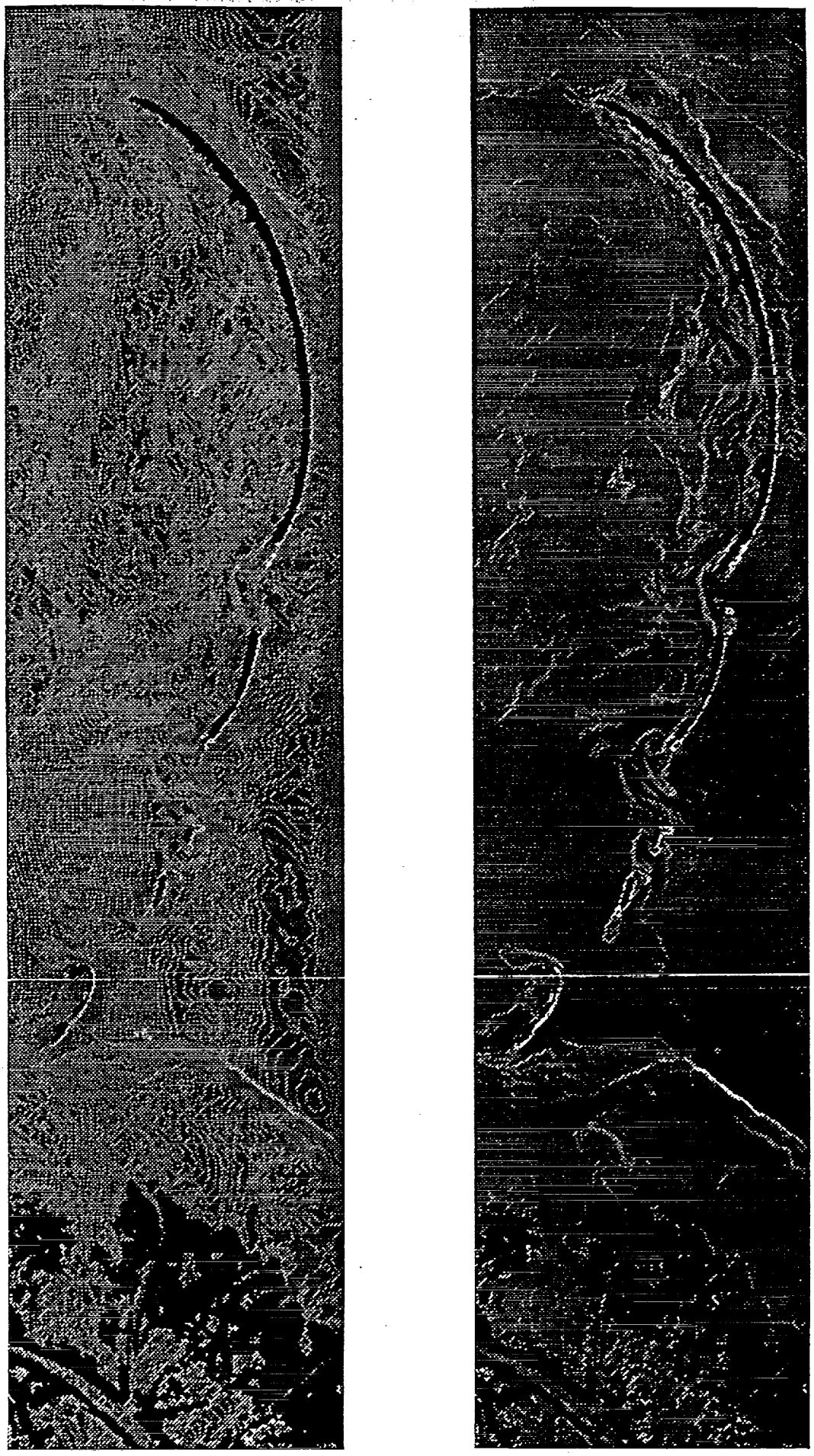

(a) (b)

Figure 3

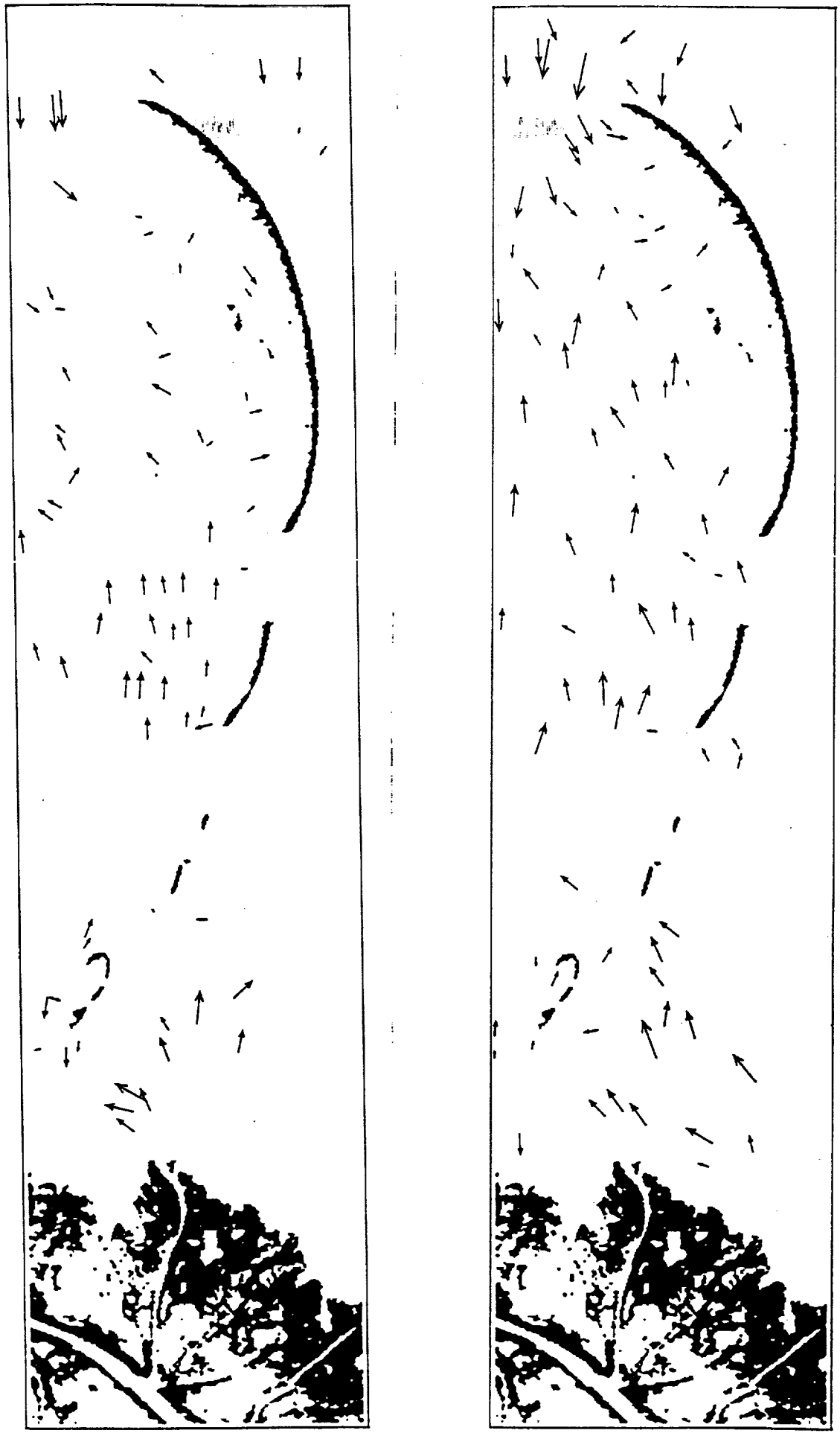

(a) (b)

Figure 4

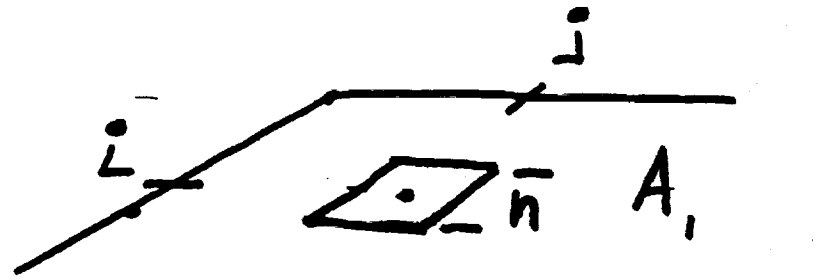

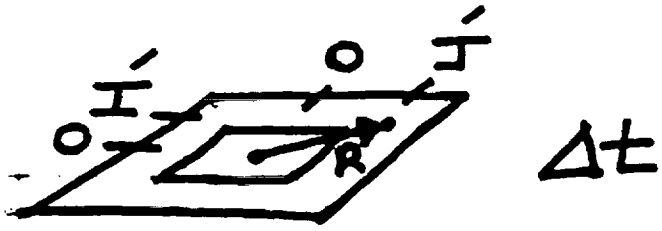

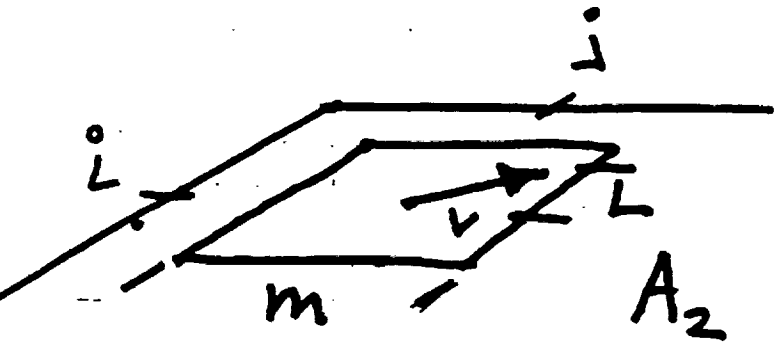

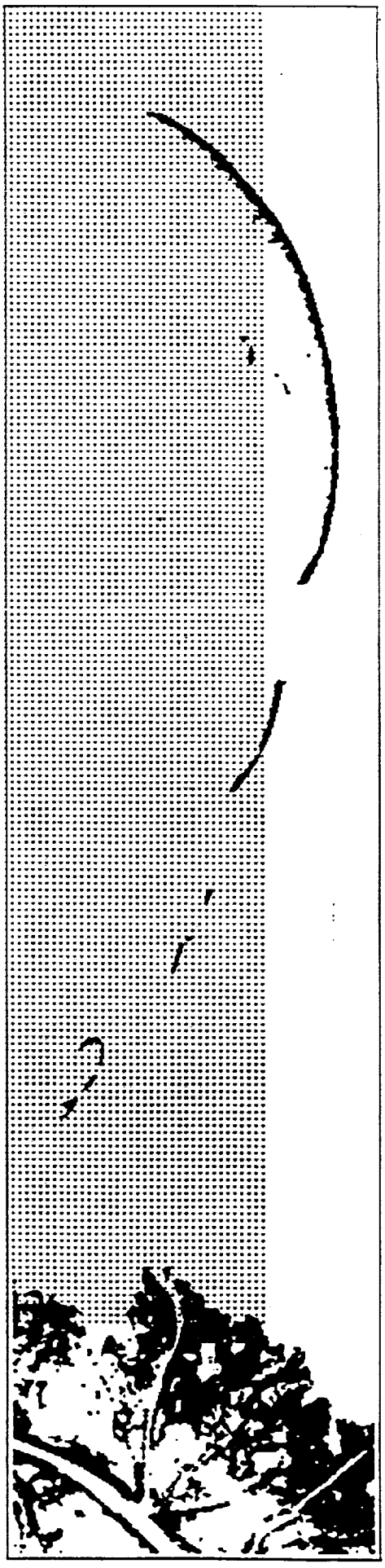

(a) Figure 5 (b)

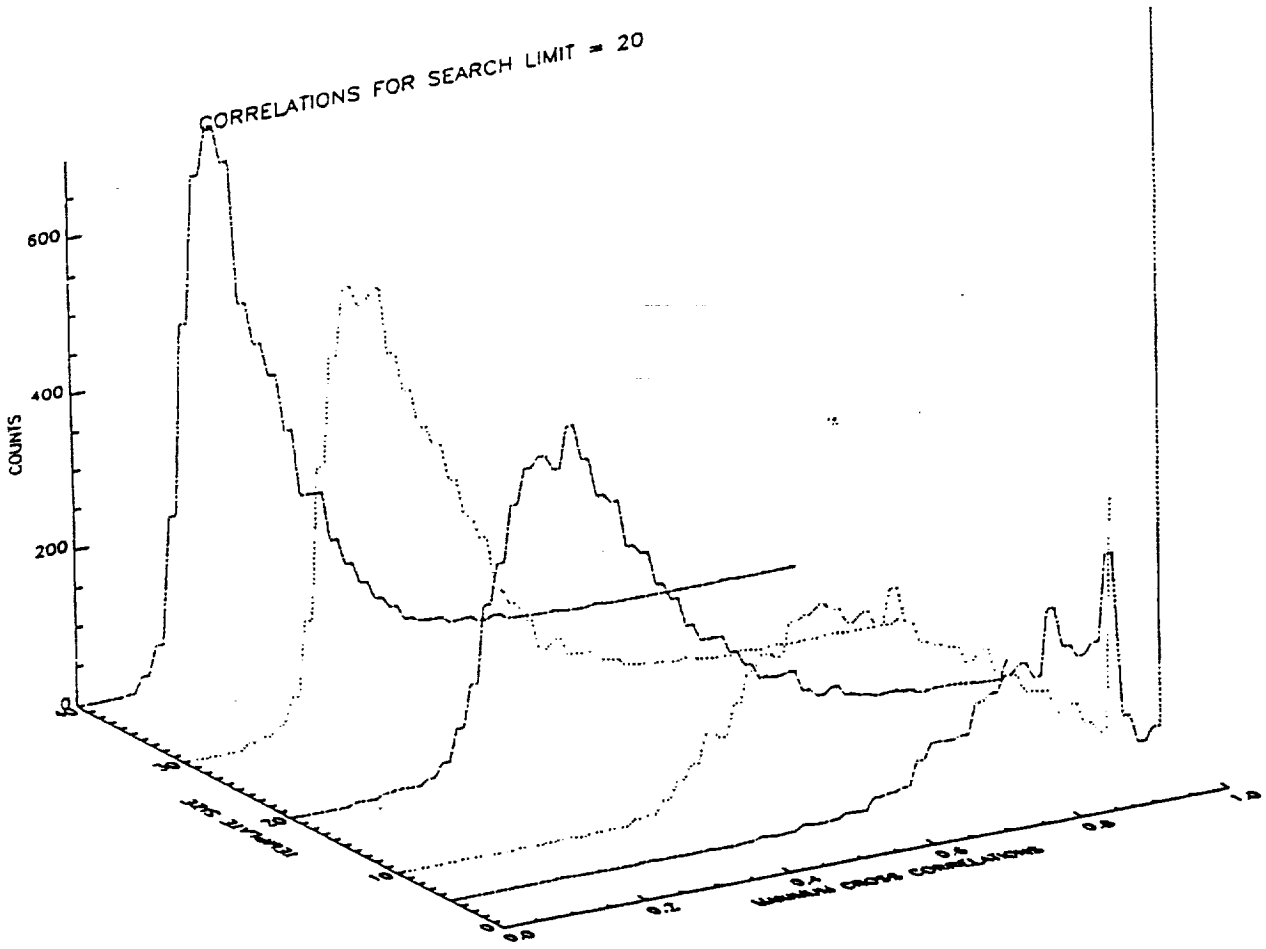
CORRELATIONS FOR SEARCH LIMIT = 20
COUNTS
600
400
200
0
0.2
0.4
0.8

Figure 6

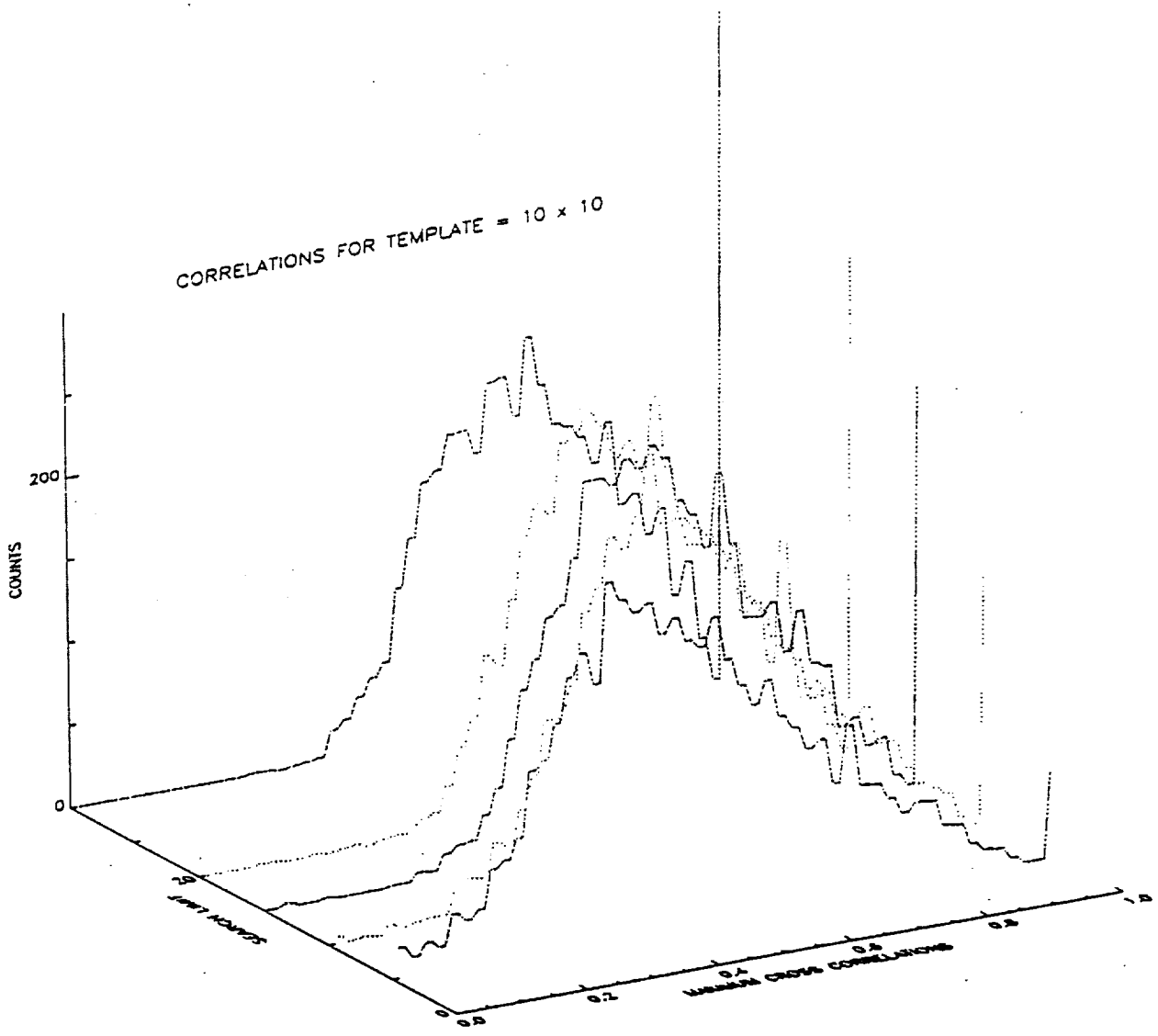

Figure 7

(a) (b)

Figure 8

(a) (b)

Figure 9

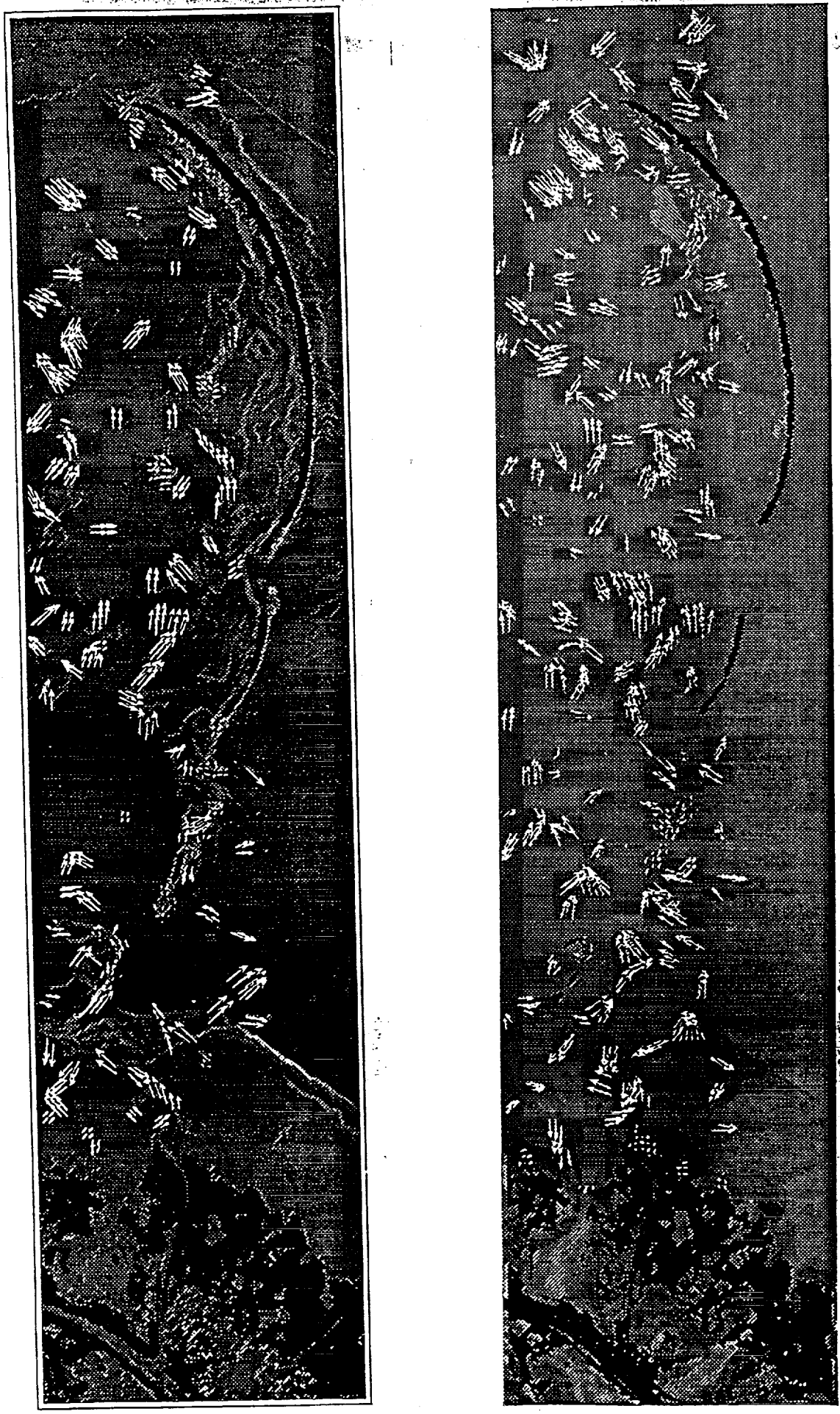

(a) (b)

Figure 10